

Detuning Axis Pulsed Spectroscopy of Valley-Orbital States in Si/SiGe Quantum Dots

Edward H. Chen,^{*} Kate Raach, Andrew Pan, Andrey A. Kiselev, Edwin Acuna, Jacob Z. Blumoff, Teresa Brecht, Maxwell Choi, Wonill Ha, Daniel Hulbert, Michael P. Jura, Tyler Keating, Ramsey Noah, Bo Sun, Bryan J. Thomas, Matthew Borselli, C.A.C. Jackson, Matthew T. Rakher, and Richard S. Ross
HRL Laboratories, LLC, 3011 Malibu Canyon Road, Malibu, California 90265, USA
 (Dated: May 26, 2022)

Silicon quantum dot qubits must contend with low-lying valley excited states which are sensitive functions of the quantum well heterostructure and disorder; quantifying and maximizing the energies of these states are critical to improving device performance. We describe a spectroscopic method for probing excited states in isolated Si/SiGe double quantum dots using standard baseband pulsing techniques, easing the extraction of energy spectra in multiple-dot devices. We use this method to measure many valley splittings spanning multiple orbital states, quantum dots, and wafers, which are crucial for studying the effects of quantum well width and other epitaxial conditions on valley splitting. Our results suggest that narrower wells can be beneficial for improving valley splittings, but this effect can be confounded by variations in growth and fabrication conditions. These results underscore the importance of valley splitting measurements for guiding the development of Si qubits.

Electrostatically confined quantum dot (QD) spin qubits in Si/SiGe quantum wells (QWs) are a promising platform for processing quantum information [1, 2]. The valleys inherent to the Si band structure, however, can fundamentally limit the initialization, manipulation, and measurement fidelities of qubit states [3]. In a typical Si/SiGe QW design, tensile strain and spatial quantization partially break the six-fold degeneracy of the bulk Si conduction band, leaving the two lowest out-of-plane valleys. This remaining degeneracy can be lifted by sharp disruptions of the periodic crystal potential at the QW interfaces. Measuring, understanding, and increasing the resulting valley splitting (VS) energy is critical for improving qubit performance.

Macroscopic magnetotransport measurements, such as Shubnikov-de Haas oscillations, are often used to probe the spectrum of large ensembles of electrons, but their relevance for few-electron QDs remains poorly understood [4–7]. Several spectroscopy methods for QDs have been demonstrated, with various advantages and limitations. Photon-assisted tunneling and other RF-based techniques are constrained by deliverable microwave frequencies, bounding the measurable energies [8, 9]. Pulsed-gate techniques can also be used to detect excited valley states, often in concert with large magnetic fields via addition energy shifts or hot-spot effects, and do not require microwave control [10–12]. However, these methods, like those based on transport, rely on electron tunneling to a neighboring electron bath, restricting the QD biasing and introducing potential ambiguities due to weakly quantized bath excitations [13, 14]. A wide range of valley splittings between 10 and 270 μeV has been measured in Si/SiGe QDs using these and other methods [15–17] and the large variation is commonly assumed

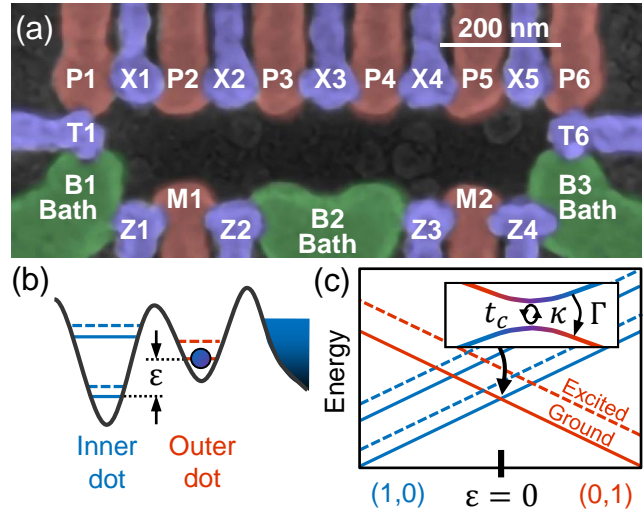


FIG. 1. (a) Scanning electron micrograph of a six QD accumulation-mode device layout typical of those used in this study. Readout is done via the M1 and M2 QDs biased to the Coulomb blockade regime to measure the charge configuration. (b) Schematic of low-energy excited states of a double quantum dot; each orbital excitation (solid lines) has an associated valley excitation (dashed lines). The detuning energy ϵ is the primary degree of freedom for extracting energy splittings in the DAPS technique. (c) Illustration of the double-dot energy level diagram along the detuning axis. The inset shows the vicinity of a level anticrossing, where the charge transfer dynamics are strongly impacted by the tunnel coupling t_c and inter-dot dephasing and relaxation rates, κ and Γ .

to be related to the QW epitaxy, though further insight is difficult as values are typically reported for just one or two QDs.

Valley splitting is sensitive to the overlap of the confined electron wave function with the Si/SiGe epitaxial

^{*} Present address: IBM Almaden Research Center, 650 Harry Road, San Jose, California 95120, USA

hetero-interfaces, and is therefore expected to improve with sharper interfaces, narrower quantum wells, and/or stronger electric fields [18–23]. Similarly, interfacial disorder originating from steps, atomic inter-diffusion, intrinsic alloy randomness, and other sources is expected to introduce valley-orbit mixing [24]. Reliable valley splitting measurements across a range of QDs and devices are necessary for disentangling these effects.

In this Letter, we introduce an experimental technique for measuring the excited state energy spectra of pairs of QDs. This method, which we call detuning axis pulsed spectroscopy (DAPS), can be applied to any charge configuration, but we primarily focus on the single-electron case for which the spectra is most easily understood. This allows us to systematically probe multiple valley and orbital states of individual dots in Si/SiGe QWs with varied widths and growth conditions. Our results validate the scalability of the DAPS technique and emphasize the importance of epitaxial uniformity for controlling the valley splitting in QD devices.

This technique probes the double QD (DQD) energy spectra by preparing electrons in the ground state of one dot and tracking charge transitions to the other dot as a function of detuning across the (1,0)-(0,1) charge boundary. Energies are extracted by identifying level anti-crossings from their enhanced charge transition rates. This requires only standard baseband control, like that used for exchange-only qubit manipulation, without RF or magnetic fields, and improves on standard pulsed-gate spectroscopy [10] by probing multiple dots without requiring direct coupling to an electron bath. We illustrate the experimental procedure in Fig. 2(a)-(b) using the (1,0)-(0,1) transition of a DQD formed in this case underneath gates P2 and P3 in Fig. 1(a). The experiment cycles between three bias points: at point ‘A’ near the (1,0) loading line, we prepare the electron in the ground state of one dot (here, P2); this can be done by waiting for thermalization within the charge cell, though we accelerate this process by allowing electron exchange with a neighboring bath extended by biasing the P1 QD to the same chemical potential as bath B1 [25]. The electron is then pulsed to point ‘B’ where the nearest dot charge sensor (DCS), either M1 or M2, is measured to record a reference conductance for the (1,0) charge state. A diabatic pulse takes the electron to point ‘C’ along the detuning axis, ϵ , across the charge boundary, where it is held for time t_{Hold} before being rapidly brought back to ‘B’ for a second charge measurement to obtain a differential signal compared to the reference. Sweeping the detuning position ‘C’ and t_{Hold} allows us to map out the charge decay dynamics, as shown in Fig. 2(c). At short hold times (e.g., $t_{Hold} = 100$ ns), sharp peaks appear due to transitions to (0,1) energy levels in the P3 dot. The detuning voltage is translated to energy using the measured gate lever arm matrix [14]; uncertainties in the latter constitute the main source of systematic error, which can be reduced by auxiliary RF measurements when available (See App. E). The procedure may

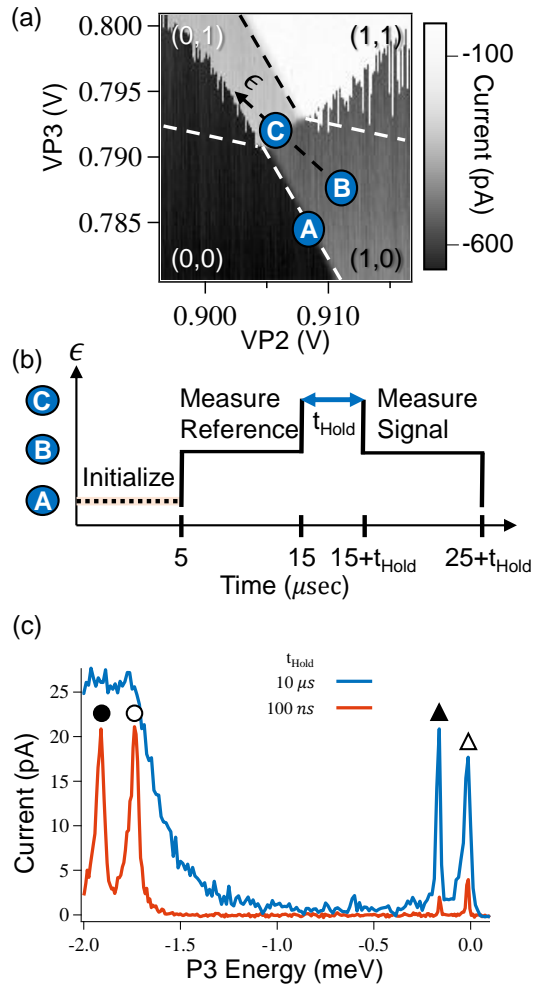


FIG. 2. (a) Measured charge stability diagram of a P2-P3 DQD. The M1 DCS conductance is measured while the voltage biases applied to P2 and P3 gates are swept. Relevant bias locations for the DAPS measurement are overlaid; the line along ‘B’-‘C’ defines the detuning axis parameterized by ϵ . (b) Pulse timing sequence for DAPS. A $5 \mu\text{s}$ initialization at ‘A’ is followed by a $10 \mu\text{s}$ charge reference measurement at ‘B’. Then the bias moves to the swept position ‘C’ for a duration t_{Hold} before a final charge measurement at ‘B’ lasting for $10 \mu\text{s}$. (c) Resulting DAPS measurement for the quantum dot underneath plunger P3 for two hold times: 100 ns (orange) and $10 \mu\text{s}$ (blue). Two orbital excited states (empty circle: ground valley; filled circle: excited valley) are resolved as peaks for $t_{Hold} = 100$ ns, but become indistinguishable for $t_{Hold} = 10 \mu\text{s}$ due to rapid inter-dot relaxation at large detuning. In contrast, the two orbital ground states (empty triangle: ground valley; filled triangle: excited valley) remain well-resolved for both hold times. These four transitions resemble states of the ‘inner’ dot illustrated in Fig. 1(b).

be modified to probe the other dot (P2 in this example) by preparing the electron at ‘A’ and adiabatically ramping across the charge boundary to the (0,1) charge cell, from where diabatic detuning excursions back into P2 can be used to extract the (1,0) spectrum. App. B

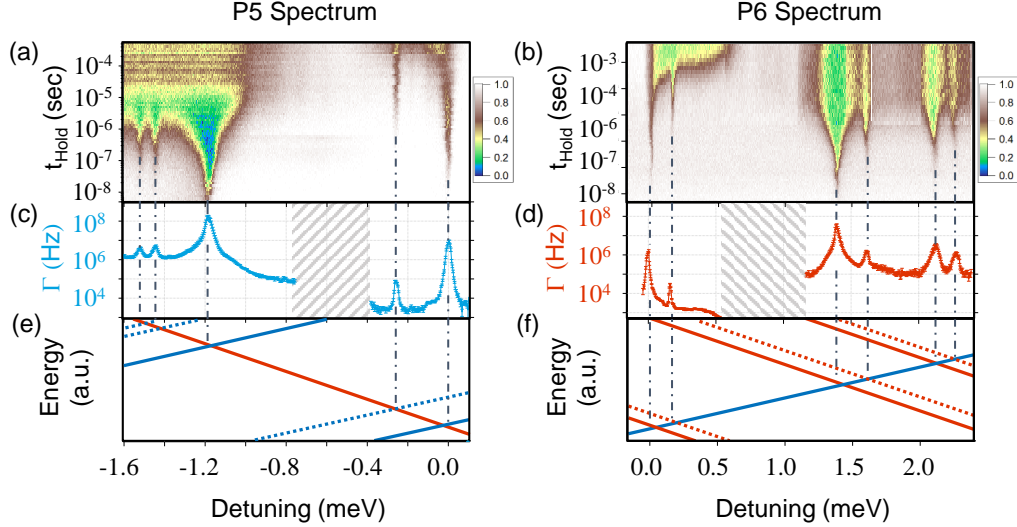


FIG. 3. DAPS charge decay measurements of a P5-P6 DQD as a function of detuning (ϵ) and hold time t_{Hold} for (a) the “inner” dot P5 and (b) the “outer” dot P6. The colorscale indicates probability of the electron remaining in its initial charge state. (c,d) Charge decay rates Γ vs detuning extracted from exponential fits of each column of the data in (a,b). (e,f) Inferred energy levels vs detuning for the P5 (blue) and P6 (red) QDs. Notably, the attributed valley ground states (solid lines) decay more quickly than their valley excited counterparts (dotted), although the second excited orbital state for P5 is not clearly observed.

discusses such an example.

This sequence resembles standard charge qubit control techniques and its dynamics can be described by a Lindblad master equation analysis where the most relevant quantities are the interdot tunnel coupling t_C , charge dephasing κ , and the interdot inelastic relaxation rate Γ , as sketched in Fig. 1(c) and discussed in greater detail in App. C. However, coherent charge manipulation requires large tunnel coupling ($\gg 1$ GHz) and hence ultrafast control. While non-adiabatic pulses can coherently probe excited states using Landau-Zener interferometry [26, 27], their extreme sensitivity to tunnel coupling and the pulse waveform can be unwieldy to optimize for spectroscopy. Instead, we find the low tunnel coupling regime to be desirable for DAPS because it maintains the diabaticity of detuning pulses, ensuring all charge transitions occur during the hold step (point ‘C’ in Fig. 2(b)). In this incoherent regime, when the DQD is detuned at an inter-dot level crossing, charge transitions occur at a rate approximately equal to t_C^2/κ where both t_C and κ can range from 0.01-10 GHz. These longer time scales are easily probed using typical control hardware for exchange-only operation, which requires bandwidths in the 0.1-1.0 GHz range [28]. To resolve these transitions, hold times should be kept short to prevent inelastic decay ($\Gamma \approx 1$ kHz-100 MHz) from equilibrating the DQD. The measurement steps at point ‘B’ must also be done faster than Γ to resolve the signal. This implies that DAPS should be performed for $\kappa t_C^{-2} < t_{Hold} < \Gamma^{-1}$. Meeting these criteria requires tuning both the tunnel

barrier and t_{Hold} , since t_C varies for excited states and the inelastic decay rate may itself be a function of detuning and tunnel coupling; Fig. 2(c) shows how the excited orbital states at large detuning are unresolved at long t_{Hold} due to faster thermalization.

Fig. 3(a,b) depicts the measured charge transition probabilities of a P5-P6 DQD versus detuning energy and hold time. Resonant peaks are identified in Fig. 3(c,d) from fitted exponential decay rates as a function of detuning, which we then associate with the level crossings illustrated in Fig. 3(e,f). Table I lists the extracted energies and approximate assignments to valley-orbit states based on the splitting magnitudes and transition strengths. In particular, the lowest excited-valley transitions exhibit decay times roughly ten times longer than the ground-valley transitions in Fig. 3(c,d), suggestive of a 3x or greater reduction of the inter-valley tunnel coupling due to differences in the inter-dot valley phase [29]. This pattern also recurs for several higher excited states, motivating our valley-orbit assignments. Nonetheless these labels can be ambiguous at high energies where multiple valley-orbit excitations are present. This is particularly so for P5, where only one “orbital-like” state with fast decay is observed compared to two “valley-like” states with slower decay rates; this could be because another state overlaps or otherwise hybridizes with the visible levels, or possibly because it lies beyond the probed energy range.

The extracted VS of $162 \mu\text{eV}$ for P6 is close to the singlet-triplet (ST) splitting of $142 \mu\text{eV}$ measured separately using two-electron spin blockade spectroscopy [15],

TABLE I. Valley splittings of ground and orbital excited states for dots P5 and P6 extracted from Fig. 3. Asterisk for second excited valley of P5 denotes ambiguity of that transition discussed in main text. See App. I for values of other energies, including orbital splittings.

Orbital State	Valley Splitting (P5) (μeV)	Valley Splitting (P6) (μeV)
Ground	260 ± 11	162 ± 10
1st excited	261 ± 14	222 ± 23
2nd excited	$336 \pm 15^*$	150 ± 27

suggesting the latter is valley-limited for this dot tune-up. We also find good agreement across multiple excited states of P6 between DAPS and pulsed-gate measurements [10], as shown in App. D. In contrast to DAPS, the latter measurement requires direct loading from an electron reservoir and hence cannot be done on interior dots (like P5) without substantial retuning.

Using the DAPS technique, we characterize *en masse* QDs in several devices fabricated on wafers grown with target QW widths from 3 to 8 nm [30]. The QW widths were confirmed to be close to their targets with X-ray reflectometry. With this larger data set of extracted energies from DAPS, we can examine the reproducibility of measured values across devices from different wafers, dots within each device, excited states within each dot, and variations with heterostructure parameters. Fig. 4 compiles the ground orbital valley splitting from 31 QDs, grouped by wafer. The largest valley splitting here of $286 \pm 26 \mu\text{eV}$ is on par with the highest previously reported in the literature for Si/SiGe QDs (which was in a depletion-mode device) [11].

For comparison, we also plot the dependence of valley splitting on well width and interface sharpness as predicted by empirical full-band tight-binding calculations [31]. These calculations assume an unbiased QW, as we expect a small out-of-plane electric field in our devices, and a smooth back interface, as obtained from previous characterization studies [32]. In general, values fall below the predictions for the atomically sharp interface, suggesting some modest degree of interfacial broadening. While interface sharpness is a convenient modeling parameter, many other factors strongly affect the predicted VS, as discussed in more detail in App. A. As a result, the exact sharpness of experimental heterostructures cannot be quantified from the theoretical curves in Fig. 4; the latter are only intended to illustrate the qualitative importance of interface quality on VS. The tendency of measurements from the same wafer to cluster, especially for wider wells, suggests that differences between epitaxial wafers contribute to the observed variation. Inter-dot variations in valley splitting are most apparent for the 3 nm well devices, suggestive of increased overlap of the electron wave function in narrower wells with a micro-

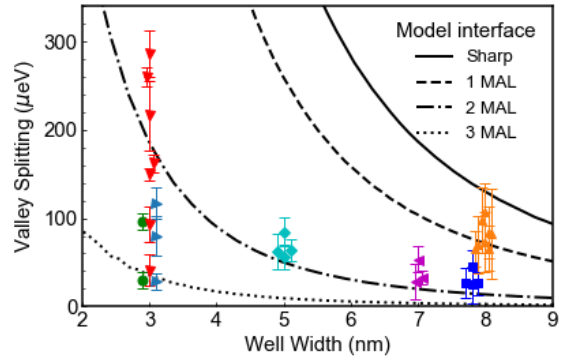


FIG. 4. Ground orbital valley splittings of 31 QDs from devices across seven wafers differentiated by symbol color and shape. The Si well widths span 3, 5, 7, and 8 nm; QDs with similar VS at the same well width are slightly displaced for visual clarity. Error bars are extracted from half-width half-maximum (HWHM) of Lorentzian fits of the extracted peaks similar to Figs. 2 and 3. Black curves correspond to tight-binding predictions of valley splitting versus well width as a function of front interface sharpness in units of mono-atomic-layer (MAL), as described in the text and App. A.

scopically inhomogeneous interface. This is consistent with the observation shown in App. F that the valley splitting can sometimes vary substantially as the electron is translated along the QW via electrostatic bias [12]. Another consequence of this disorder is that the valley splitting of different orbitals within the same dot also tends to vary, as suggested by Table I and further supported by measurements on multiple dots in App. G.

We have presented a technique for mapping out the energy spectra of electrostatically defined quantum dots and applied it to measure ground and excited orbital valley splittings of an assortment of Si/SiGe QDs tuned close to their intended operating regime. The relative ease of the DAPS method allows probing of valley splitting disorder within and between QDs as well as different wafers, which will be critical for identifying and improving optimal epitaxial conditions for Si/SiGe qubits. The largest splittings in our results were observed in 3 nm well devices, though further work is needed to fully understand all other sources of variations. We note that the well widths explored here are narrower than typically used for Si/SiGe qubits in other works (8-18 nm), but have found this does not prevent the formation or hinder the performance of spin qubits [33–35]. Although we have presented single-electron measurements in this work, the DAPS technique can be extended to study multi-electron state spectra since it relies on the general effects of charge dephasing and relaxation, such as the two-electron spectra extraction discussed in App. H. Our approach may also be applicable for studying the rich interplay of the orbital, valley, and spin degrees of freedom in quantum dot states in other systems besides Si/SiGe, such as Si

The authors thank Emily Pritchett, Seth Merkel, Sean Meenehan, and Sieu Ha for valuable discussions.

- [1] L. M. Vandersypen and M. A. Eriksson, Quantum computing with semiconductor spins, *Physics Today* **72**, 38 (2019).
- [2] T. D. Ladd and M. S. Carroll, Silicon qubits, in *Encyclopedia of Modern Optics (Second Edition)*, edited by B. D. Guenther and D. G. Steel (Elsevier, Oxford, 2018) second edition ed., pp. 467 – 477.
- [3] F. A. Zwanenburg, A. S. Dzurak, A. Morello, M. Y. Simmons, L. C. L. Hollenberg, G. Klimeck, S. Rogge, S. N. Coppersmith, and M. A. Eriksson, Silicon quantum electronics, *Rev. Mod. Phys.* **85**, 961 (2013).
- [4] S. Goswami, K. Slinker, M. Friesen, L. McGuire, J. Truitt, C. Tahan, L. Klein, J. Chu, P. Mooney, D. W. Van Der Weide, *et al.*, Controllable valley splitting in silicon quantum devices, *Nature Physics* **3**, 41 (2007).
- [5] K. Sasaki, R. Masutomi, K. Toyama, K. Sawano, Y. Shiraki, and T. Okamoto, Well-width dependence of valley splitting in si/sige quantum wells, *Applied Physics Letters* **95**, 222109 (2009).
- [6] S. F. Neyens, R. H. Foote, B. Thorgrimsson, T. Knapp, T. McJunkin, L. Vandersypen, P. Amin, N. K. Thomas, J. S. Clarke, D. Savage, *et al.*, The critical role of substrate disorder in valley splitting in si quantum wells, *Applied Physics Letters* **112**, 243107 (2018).
- [7] B. P. Wuetz, M. P. Losert, A. Tosato, M. Lodari, P. L. Bavdaz, L. Stehouwer, P. Amin, J. S. Clarke, S. N. Coppersmith, A. Sammak, *et al.*, Effect of quantum hall edge strips on valley splitting in silicon quantum wells, arXiv preprint arXiv:2006.02305 (2020).
- [8] K. Wang, C. Payette, Y. Dovzhenko, P. Deelman, and J. R. Petta, Charge relaxation in a single-electron si/sige double quantum dot, *Physical review letters* **111**, 046801 (2013).
- [9] X. Mi, C. G. Péterfalvi, G. Burkard, and J. R. Petta, High-resolution valley spectroscopy of si quantum dots, *Phys. Rev. Lett.* **119**, 176803 (2017).
- [10] J. Elzerman, R. Hanson, L. Willems van Beveren, L. Vandersypen, and L. Kouwenhoven, Excited-state spectroscopy on a nearly closed quantum dot via charge detection, *Applied Physics Letters* **84**, 4617 (2004).
- [11] M. G. Borselli, R. S. Ross, A. A. Kiselev, E. T. Croke, K. S. Holabird, P. W. Deelman, L. D. Warren, I. Alvarado-Rodriguez, I. Milosavljevic, F. C. Ku, *et al.*, Measurement of valley splitting in high-symmetry si/sige quantum dots, *Applied Physics Letters* **98**, 123118 (2011).
- [12] A. Hollmann, T. Struck, V. Langrock, A. Schmidbauer, F. Schauer, K. Sawano, H. Riemann, N. V. Abrosimov, D. Bougeard, and L. R. Schreiber, Large and tunable valley splitting in si/sige quantum dots, *Physical Review Applied* **13**, 034068 (2020).
- [13] M. Fuechsle, S. Mahapatra, F. Zwanenburg, M. Friesen, M. Eriksson, and M. Y. Simmons, Spectroscopy of few-electron single-crystal silicon quantum dots, *Nature Nanotechnology* **5**, 502 (2010).
- [14] C. Simmons, J. Prance, B. Van Bael, T. S. Koh, Z. Shi, D. Savage, M. Lagally, R. Joynt, M. Friesen, S. Coppersmith, *et al.*, Tunable spin loading and T_1 of a silicon spin qubit measured by single-shot readout, *Physical review letters* **106**, 156804 (2011).
- [15] A. Jones, E. Pritchett, E. Chen, T. Keating, R. Andrews, J. Blumoff, L. De Lorenzo, K. Eng, S. Ha, A. Kiselev, S. Meenehan, S. Merkel, J. Wright, L. Edge, R. Ross, M. Rakher, M. Borselli, and A. Hunter, Spin-blockade spectroscopy of Si/Si-Ge quantum dots, *Phys. Rev. Applied* **12**, 014026 (2019).
- [16] J. S. Schoenfield, B. M. Freeman, and H. Jiang, Coherent manipulation of valley states at multiple charge configurations of a silicon quantum dot device, *Nature communications* **8**, 1 (2017).
- [17] N. Penthorn, J. Schoenfield, J. Rooney, L. Edge, and H. Jiang, Two-axis quantum control of a fast valley qubit in silicon, *npj Quantum Information* **5**, 1 (2019).
- [18] T. B. Boykin, G. Klimeck, M. Eriksson, M. Friesen, S. Coppersmith, P. Von Allmen, F. Oyafuso, and S. Lee, Valley splitting in strained silicon quantum wells, *Applied Physics Letters* **84**, 115 (2004).
- [19] T. B. Boykin, G. Klimeck, M. Friesen, S. Coppersmith, P. von Allmen, F. Oyafuso, and S. Lee, Valley splitting in low-density quantum-confined heterostructures studied using tight-binding models, *Physical Review B* **70**, 165325 (2004).
- [20] M. Friesen, S. Chutia, C. Tahan, and S. Coppersmith, Valley splitting theory of si ge/ si/ si ge quantum wells, *Physical Review B* **75**, 115318 (2007).
- [21] N. Kharche, M. Prada, T. B. Boykin, and G. Klimeck, Valley splitting in strained silicon quantum wells modeled with 2 miscuts, step disorder, and alloy disorder, *Applied Physics Letters* **90**, 092109 (2007).
- [22] L. Zhang, J.-W. Luo, A. Saraiva, B. Koiller, and A. Zunger, Genetic design of enhanced valley splitting towards a spin qubit in silicon, *Nature Communications* **4**, 2396 (2013), article.
- [23] N. M. Zimmerman, P. Huang, and D. Culcer, Valley phase and voltage control of coherent manipulation in si quantum dots, *Nano letters* **17**, 4461 (2017).
- [24] J. K. Gamble, M. Eriksson, S. Coppersmith, and M. Friesen, Disorder-induced valley-orbit hybrid states in si quantum dots, *Physical Review B* **88**, 035310 (2013).
- [25] B. M. Maune, M. G. Borselli, B. Huang, T. D. Ladd, P. W. Deelman, K. S. Holabird, A. A. Kiselev, I. Alvarado-Rodriguez, R. S. Ross, A. E. Schmitz, M. Sokolich, C. A. Watson, M. F. Gyure, and A. T. Hunter, Coherent singlet-triplet oscillations in a silicon-based double quantum dot, *Nature* **481**, 344 (2012).
- [26] J. S. Schoenfield, B. M. Freeman, and H. Jiang, Coherent manipulation of valley states at multiple charge configurations of a silicon quantum dot device, *Nature Communications* **8**, 64 (2017).
- [27] X. Mi, S. Kohler, and J. Petta, Electrically protected

- valley-orbit qubits in silicon, *Physical Review B* **98**, 164404 (2018).
- [28] M. D. Reed, B. M. Maune, R. W. Andrews, M. G. Borselli, K. Eng, M. P. Jura, A. A. Kiselev, T. D. Ladd, S. T. Merkel, I. Milosavljevic, E. J. Pritchett, M. T. Rakher, R. S. Ross, A. E. Schmitz, A. Smith, J. A. Wright, M. F. Gyure, and A. T. Hunter, Reduced sensitivity to charge noise in semiconductor spin qubits via symmetric operation, *Phys. Rev. Lett.* **116**, 110402 (2016).
- [29] D. Culcer, L. Cywiński, Q. Li, X. Hu, and S. Das Sarma, Quantum dot spin qubits in silicon: Multivalley physics, *Phys. Rev. B* **82**, 155312 (2010).
- [30] H. Sigg, C. Falub, E. Müller, A. Borak, D. Grützmacher, T. Fromherz, M. Meduna, and O. Kermarrec, Bandstructure analysis of strain compensated si/sige quantum cascade structures, *Optical Materials* **27**, 841 (2005).
- [31] Y.-M. Niquet, D. Rideau, C. Tavernier, H. Jaouen, and X. Blase, Onsite matrix elements of the tight-binding hamiltonian of a strained crystal: Application to silicon, germanium, and their alloys, *Physical Review B* **79**, 245201 (2009).
- [32] O. Dyck, D. N. Leonard, L. F. Edge, C. A. Jackson, E. J. Pritchett, P. W. Deelman, and J. D. Poplawsky, Accurate quantification of si/sige interface profiles via atom probe tomography, *Advanced Materials Interfaces* **4**, 1700622 (2017).
- [33] R. W. Andrews, C. Jones, M. D. Reed, A. M. Jones, S. D. Ha, M. P. Jura, J. Kerckhoff, M. Levendorf, S. Meenehan, S. T. Merkel, A. Smith, B. Sun, A. J. Weinstein, M. T. Rakher, T. D. Ladd, and M. G. Borselli, Quantifying error and leakage in an encoded Si/SiGe triple-dot qubit, *Nature nanotechnology* **14**, 747 (2019).
- [34] B. Sun, Full permutation dynamical decoupling in an encoded triple-dot qubit, *Bulletin of the American Physical Society* (2020).
- [35] J. Blumoff, Quantifying high-fidelity state preparation and measurement in triple-quantum-dot qubits, *Bulletin of the American Physical Society* (2020).
- [36] J. K. Gamble, P. Harvey-Collard, N. T. Jacobson, A. D. Baczewski, E. Nielsen, L. Maurer, I. Montaña, M. Rudolph, M. S. Carroll, C. H. Yang, A. Rossi, A. S. Dzurak, and R. P. Muller, Valley splitting of single-electron si mos quantum dots, *Applied Physics Letters* **109**, 253101 (2016), <https://doi.org/10.1063/1.4972514>.
- [37] J. R. Petta, A. C. Johnson, C. M. Marcus, M. P. Hanson, and A. C. Gossard, Manipulation of a single charge in a double quantum dot, *Phys. Rev. Lett.* **93**, 186802 (2004).
- [38] K. Wang, K. De Greve, L. A. Jauregui, A. Sushko, A. High, Y. Zhou, G. Scuri, T. Taniguchi, K. Watanabe, M. D. Lukin, *et al.*, Electrical control of charged carriers and excitons in atomically thin materials, *Nature nanotechnology* **13**, 128 (2018).
- [39] M. Friesen, S. Chutia, C. Tahan, and S. N. Coppersmith, Valley splitting theory of SiGe/Si/SiGe quantum wells, *Phys. Rev. B* **75**, 115318 (2007).
- [40] M. Nestoklon, E. Ivchenko, J.-M. Jancu, and P. Voisin, Electric field effect on electron spin splitting in si ge/ si quantum wells, *Physical Review B* **77**, 155328 (2008).
- [41] L. Zhang, J.-W. Luo, A. Saraiva, B. Koiller, and A. Zunger, Genetic design of enhanced valley splitting towards a spin qubit in silicon, *Nature communications* **4**, 1 (2013).
- [42] Z. Jiang, N. Kharche, T. Boykin, and G. Klimeck, Effects of interface disorder on valley splitting in sige/si/sige quantum wells, *Applied Physics Letters* **100**, 103502 (2012).
- [43] T. B. Boykin, G. Klimeck, M. A. Eriksson, M. Friesen, S. N. Coppersmith, P. von Allmen, F. Oyafuso, and S. Lee, Valley splitting in strained silicon quantum wells, *Applied Physics Letters* **84**, 115 (2004), <https://doi.org/10.1063/1.1637718>.
- [44] J.-M. Jancu and P. Voisin, Tetragonal and trigonal deformations in zinc-blende semiconductors: A tight-binding point of view, *Physical Review B* **76**, 115202 (2007).
- [45] F. Sacconi, A. Di Carlo, P. Lugli, M. Stadele, and J.-M. Jancu, Full band approach to tunneling in mos structures, *IEEE Transactions on Electron Devices* **51**, 741 (2004).
- [46] L. S. Langsjoen, A. Poudel, M. G. Vavilov, and R. Joynt, Qubit relaxation from evanescent-wave johnson noise, *Physical Review A* **86**, 010301 (2012).
- [47] C. Tahan and R. Joynt, Relaxation of excited spin, orbital, and valley qubit states in ideal silicon quantum dots, *Physical Review B* **89**, 075302 (2014).
- [48] A. Seedhouse, T. Tanttu, R. C. Leon, R. Zhao, K. Y. Tan, B. Hensen, F. E. Hudson, K. M. Itoh, J. Yoneda, C. H. Yang, *et al.*, Parity readout of silicon spin qubits in quantum dots, arXiv preprint arXiv:2004.07078 (2020).
- [49] Z. Shi, C. B. Simmons, D. R. Ward, J. R. Prance, R. T. Mohr, T. S. Koh, J. K. Gamble, X. Wu, D. E. Savage, M. G. Lagally, M. Friesen, S. N. Coppersmith, and M. A. Eriksson, Coherent quantum oscillations and echo measurements of a si charge qubit, *Phys. Rev. B* **88**, 075416 (2013).
- [50] D. P. DiVincenzo, D. Bacon, J. Kempe, G. Burkard, and K. B. Whaley, Universal quantum computation with the exchange interaction, *Nature* **408**, 339 (2000).

Appendix A: Valley Splitting Modeling

We perform empirical *spds** tight-binding calculations of valley splitting to understand the theoretically expected dependence on well width. Valley splitting models for Si/SiGe QWs frequently assume perfectly abrupt interfaces, which may be interrupted by steps or tilts, as reviewed for tight-binding calculations in [3]. In the case of an electron confined by two perfectly abrupt interfaces, the valley splitting oscillates as the QW width changes at the mono-atomic-layer (MAL) scale due to inter-valley phase interference [39–41]. In general, however, growth kinetics and atomic diffusion during epitaxy and device fabrication will broaden the interfaces, as confirmed by microscopy and atom probe tomography [32]. These measurements suggest that the back interface is typically broader than the front interface, which would suppress valley interferometric effects as a function of well width. Additional asymmetries, such as the presence of a strong electric field, would similarly depress valley oscillations.

Our tight-binding calculations use the parameters for bulk Si and Ge in [31], with the $\text{Si}_{0.7}\text{Ge}_{0.3}$ layers described within the virtual crystal approximation (VCA). We model each QW interface using a sigmoidal function for the Ge concentration:

$$\chi_{\pm}(x) = \frac{\chi_{\text{SiGe}}}{1 + e^{(x_{0,\pm} \pm x)/\tau_{\pm}}} \quad (\text{A1})$$

where $x_{0,\pm}$ denote interface position and τ_{\pm} is the interface width parameter for the front and back interfaces, respectively; 4τ is the distance over which the Ge percentage varies from 12% to 88% of its value in the barrier region χ_{SiGe} . We fix $4\tau_{-}$ for the back interface at 8 MAL, following the extracted values in [32], and vary the sharpness of the front interface $4\tau_{+}$ between 0-3 MAL to obtain the results shown in Fig. 4. Zero applied vertical electric field is assumed, since electrostatic simulations of our devices indicate a negligible field under typical operating conditions. In general, a finite positive electric field will tend to increase the valley splitting as the electron overlaps more strongly with the sharp front interface; this effect is more prominent for wider well widths.

While the τ_{+} of the front interface is the only free parameter in our calculations, in practice a large number of additional factors will affect the predicted VS values. Our calculations are for 1-D QW structures and thus do not include disorder effects beyond the homogeneous smoothing of the interfaces; such disorder would further broaden the expected VS distribution [42]. Additionally, while the empirical tight-binding parameters for Si and Ge are obtained by fitting to bulk band structure features, multiple parametrizations are possible and the relevant inter-valley coupling is not uniquely constrained at present. In our experience, commonly used Si and Ge *spds** tight-binding parameter sets in the literature [43–45] can lead to variations of up to 2X in predicted VS. Furthermore, any true heterostructure is ultimately composed of substitutional Ge atoms in the barrier regions

and therefore also includes local strain. 3-D atomistic calculations including these effects can lead to quantitative differences from 1-D VCA models (as discussed in the supplemental section of [3], for example). Because of the quantitative importance and uncertainty of these and other factors in the model, these calculations are only intended to serve as a qualitative indicator of the sensitivity of VS to interface effects, not an attempt to quantify interface sharpness τ using measured VS values.

Appendix B: Peak Alignments for a DQD Pair

The DAPS technique works on a pair of adjacent dots, and irrespective of which dot the reference measurement is performed on, there is only one ground-ground anti-crossing for the dot pair. Therefore when DAPS measurements for both dots are directly compared, the expectation is the ground-ground peak locations in detuning voltage should exactly align. In practice, however, we find that the maxima of the peaks may not be quite aligned with each other as shown in Fig. A1(a). This detuning offset between the peaks persists even when the measurement is taken in terms of the relative populations

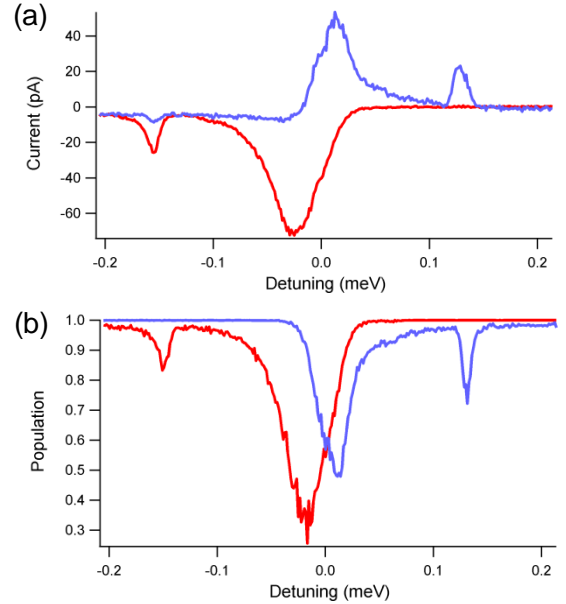


FIG. A1. (a) The P5 (red) and P6 (blue) DAPS sequences at two different hold times (6 and 0.5 μs) have opposite charge signals due to their opposite charge state references. Comparing the two reveals a detuning offset between the maxima of the ground-ground transition peaks. (b) P6 and P5 DAPS measurement sequence as in (a) except the lock-in signal is measured in terms of relative population between the reference charge state and the charge state post-dephasing. A value of 1.0 represents 100% of the population remaining in the initial charge state after dephasing at the detuning point (x-axis), while 0.0 represents 0% of the initial population remaining in the initial charge state.

between the two charge states, Fig. A1(b), and suggests the location of the anti-crossing is between the onset of the peak and the maximum of the peak. This observation can be explained by asymmetry versus detuning of inelastic charge thermalization Γ and is reproduced by modeling, as discussed in App. C, and can also be influenced by non-ideal pulses. It motivates our decision to label the uncertainty for each DAPS peak as approximately the half-width at half-maximum (HWHM) obtained from Lorentzian fits. This error can be alleviated by operating at shorter hold times to suppress inelastic decay, at the cost of reduced signal.

Appendix C: Model of DAPS Dynamics

The main dynamic features of our experiments can be captured from a standard Lindblad master equation analysis. When a DQD is detuned in the immediate vicinity of an inter-dot transition, the relevant parameters are the detuning from the anti-crossing (ϵ), the inter-dot tunnel coupling (t_C), the charge dephasing rate (κ), and inelastic decay (Γ , which is detuning dependent), so that the dynamics of the two levels of the anticrossing can be described by the density matrix evolution:

$$\dot{\rho}(t) = -i[\epsilon\sigma_z + t_C\sigma_x, \rho] - \frac{\kappa}{2}(\sigma_z\rho\sigma_z - \rho) + \mathcal{L}_{\Gamma(\epsilon)}(\rho). \quad (\text{C1})$$

It is straightforward to show that in the absence of Γ and when $\kappa > t_C$, the system decays to a 50-50 mixed charge state at a relaxation rate approximately given by $\frac{\kappa t_C^2}{\kappa^2 + \epsilon^2}$, motivating the use of a Lorentzian fit of the decay rate around each transition for determining the peak position. This yields a peak in decay rate at the anti-crossing, which is the central feature we seek; however, away from the anti-crossing, inelastic decay is necessary to thermalize the final state population to equilibrium. We describe the latter with the decay superoperator in Eq. C1, where the inelastic decay rate Γ can arise from couplings to a variety of environmental degrees of freedom, including evanescent wave Johnson noise (EWJN) from metal gates and neighboring 2DEG reservoirs [46] and acoustic phonons in Si [47]. While the precise magnitudes of the lifetimes depend sensitively on device features, we expect that at small detuning, EWJN-induced relaxation scales as $\Gamma_n \propto t_C^2/\epsilon$ while phonon-induced relaxation scales as $\Gamma_p h \propto t_C^2\epsilon^3$. Importantly, this suggests that at small and moderate DQD detuning, the inelastic decay rate may be slower than the dephasing-induced charge decay near excited state anti-crossings, allowing the latter to be resolved. At larger detuning, phonon-induced decay dominates and its magnitude must include the competing influence of phonon bottleneck effects, increased phonon density of states, and enhancement of the transition matrix elements due to the spatially extended wave functions of excited states. Numerical calculations show strong enhancement of inelastic decay in

this regime, which can make transitions at excited anti-crossings harder to pick out.

To show how these dynamics are relevant to resolving excited state energies, we extend this model to a three-level calculation of dynamics as a function of detuning and hold time as shown in Fig. A2(a), modeling the DAPS decay of the charge state of one dot into the ground and valley excited states of another dot. The calculations qualitatively reproduce the experimental decay dynamics seen at low detuning in Fig. A2(b) as well as Fig. 3(a)-(b) of the main text. One important feature of both the model and experimental results, as discussed in App. B, is that the locations corresponding to inter-dot peaks tend to shift towards positive detuning as the hold time increases; this occurs because charge relaxation Γ tends to asymmetricize the charge state population by pushing it towards thermalization. As hold time increases, the detuning location of each peak will therefore be offset from the true anti-crossing position, which will usually be located on the rising shoulder of the peak. Therefore, peak positions should ideally be extracted at short hold times for the most accurate extraction of excited state energies.

Interestingly, the extracted inelastic decay rates shown in Fig. A2(c) scale as ϵ^{-2} at small detuning. One possible reason for this discrepancy between model and experiment is that some other decay mechanism besides phonons or EWJN dominates at very low energies, as other experiments in Si/SiGe QDs have also suggested [8, 12]. While this model captures the essential features of the DAPS technique, it neglects important details such as the presence of $1/f$ charge noise, whose effects are not simply parameterized by a Markovian dephasing rate κ and may contribute to non-exponential decay and the broadening of transition peaks in experiments. Recently, a similar model has been applied to describe the dynamics of readout in singlet-triplet qubits [48].

Appendix D: Consistency of DAPS with other methods to probe excited state spectra

Although there is some uncertainty about the precise location of the transitions along the detuning axis as discussed in App. B, DAPS measurements do provide reliable relative energy scales. The excited state energies extracted from DAPS are comparable to those obtained from the commonly used pulsed-gate spectroscopy technique [10] shown in Fig. A3(a)-(c). The DAPS (162 μeV) and pulsed-gate (173 μeV) measurements of the valley splitting for P6 are generally consistent with the largest singlet-triplet splitting of 142 μeV measured on P6 using the technique in Ref. [15] shown in Fig. A3(b).

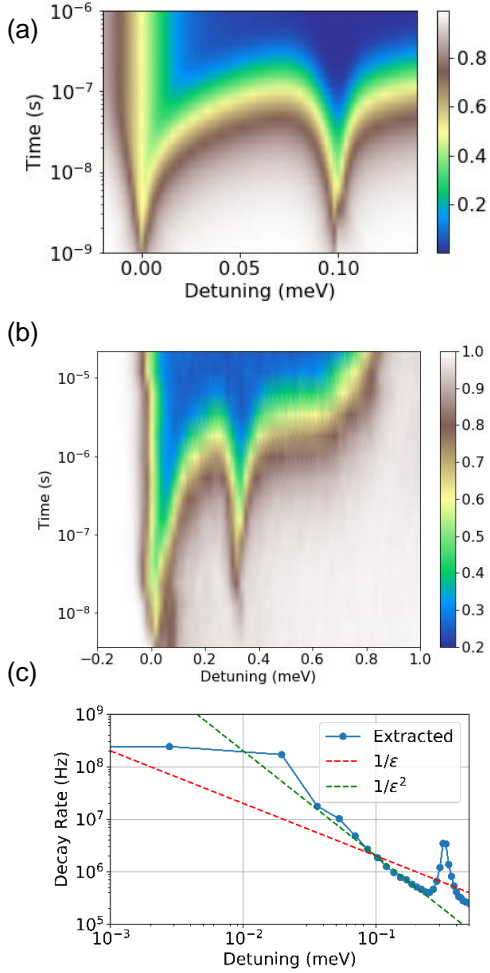
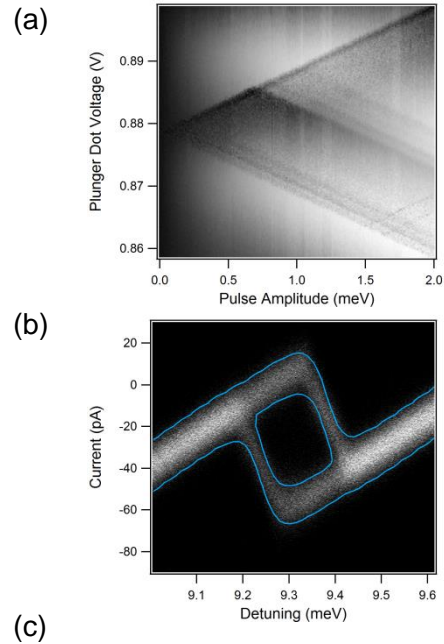


FIG. A2. (a) Theoretically calculated decay of initial (1,0) charge state as a function of detuning and hold time in a three-level model including ground and valley (0,1) states. (b) DAPS decay measurement for one QD as function of detuning and hold time in the vicinity of the ground orbital and valley transitions. (c) Extracted charge decay rate from data (b) as function of detuning; dashed lines are fits to $1/\epsilon$ and $1/\epsilon^2$ dependences showing the latter better matches the experimental dependence at low energies.

Appendix E: DAPS with continuously applied photon assisted transitions

Converting applied detuning voltages into energy scales is commonly done by synthesizing separate measurements of gate lever arms and cross-capacitances (See Appendix in [15]). This approach, although expedient, is prone to systematic errors. We address this concern by operating the DAPS sequences exactly as described in the main text while also applying a continuous-wave microwave tone to drive photon-assisted tunneling (PAT) transitions. These experiments reveal PAT transitions in the DAPS spectra (Fig. A4(b)). By sweeping the fre-

quency of the applied tone (Fig. A4(c)) and fitting a linear slope to the two frequency-dependent detuning transitions, we are able to more accurately convert detuning voltages into an energy scale by using the slope as the so-called detuning scale factor (DSF), which has units of eV per V. Sweeping both detuning and hold time with an applied CW tone reveals even more PAT transitions whose spacings are consistent with our original interpretation of the transitions as excited states in the dots, as seen in Fig. A5. The visibility of these measurements varies significantly in practice depending on the sensitivity of the QD to applied microwave tones.



1e ⁻ spectra	DAPS (μeV)	Pulsed Gate (μeV)
Valley	140	173
Orbital 1	1399	1518
Orbital 1 + Valley	1399 + 217	1518 + 188
Orbital 2	2131	2186
Orbital 2 + Valley	2131 + 150	-

FIG. A3. (a) Pulsed-gate spectroscopy on dot P6 in nearly the same electrostatic configuration as used for the DAPS sequence on P6 (Fig. 3 of main text). (b) Data set of the largest spin-blockade spectroscopy of the singlet-triplet splitting using two electrons in P6. (c) Table comparing DAPS, pulsed-gate and spin-blockade spectroscopic techniques for dot P6.

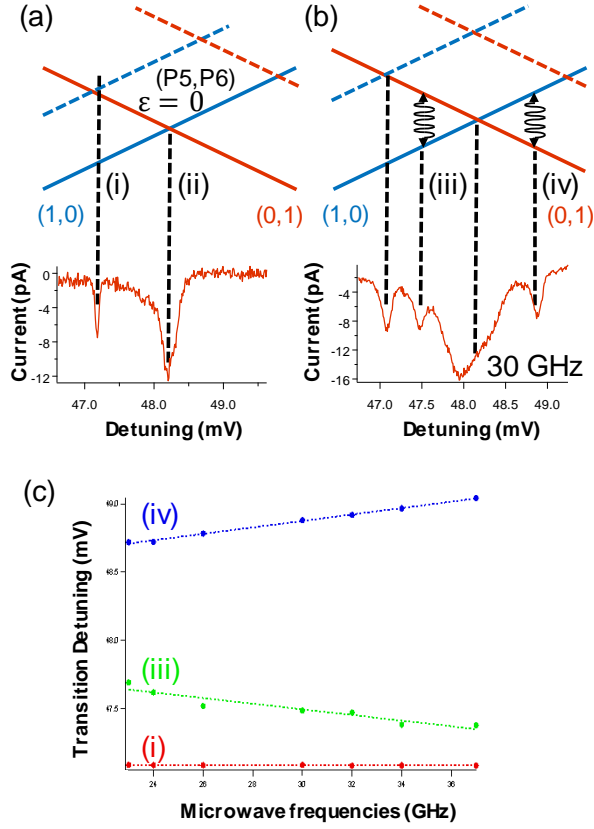


FIG. A4. (a) DAPS spectrum of QD at a hold time of 5 μ s without applying continuous microwave drive. Transition (i) is the ground-to-excited transition, while (ii) is the ground-to-ground transition. (b) Same experimental pulse sequence at a hold time of 10 μ s, with 30 GHz continuous microwave drive applied through a neighboring gate. Two new transitions, labeled as (iii) and (iv), appear due to photon-assisted tunneling. (c) Tracking transitions (i), (iii) and (iv) versus microwave frequency. The average of the slopes (blue and green) result in a detuning scale factor of 0.186 eV/V.

Appendix F: Measuring DAPS at different electrostatic bias

To observe the sensitivity of energy splittings on the electrostatic confinement, we can evaluate how much DAPS transitions are affected by changing the bias of a nearby gate (typically a neighboring tunneling barrier), which alters the convexity of the potential confinement along one of the two spatial directions and causes lateral displacement of the quantum dot along that same direction. In the ideal scenario, we expect orbital-like transitions to be more sensitive to these changes than valley-like transitions. However, the valley mixing can also experience substantial changes as the electron is translated along a microscopically varying heterointerface, due to some combination of disorder effects such as interfacial steps and/or intrinsic atomistic random alloy

fluctuations. In Fig. A6 we observe that two neighboring dots (P5 and P6 in a device) exhibit very different behavior in the measured VS as a function of bias on different adjacent gates; P5 shows significant change (by about a factor of 3X within the probed bias range) while its neighboring dot retains a roughly constant VS. This illustrates both the importance of local microscopic disorder on the VS as well as the possibility that such disorder can be uncorrelated between different dots. The trends we detect in bias tunability of VS are consistent with previous observations in the literature [12, 49].

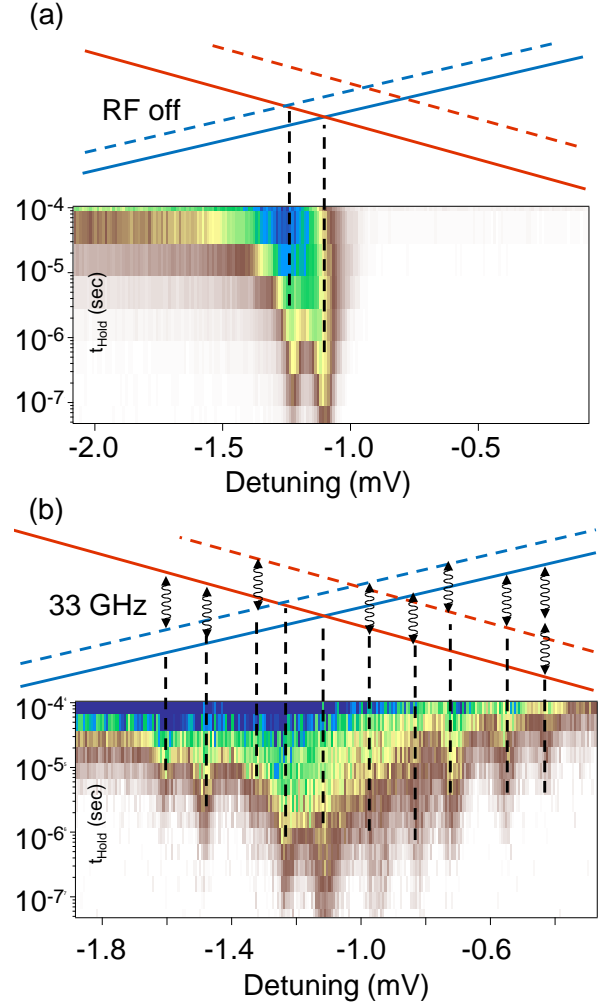


FIG. A5. (a) DAPS measurement at small detunings for a QD without RF drive. This experimental procedure is identical to those described in the main text, but with RF off. (b) DAPS measurement for same QD but with 33 GHz RF tone applied to a nearby gate. Some two-photon transitions are also visible, whose positions correspond well with the DC and RF resonances expected from the energy level diagram depicted. The faint transition on far right potentially corresponds to a two-photon resonance.

Appendix G: Valley splitting variation across orbital states

The extracted VS for different orbitals within the same dot also tends to vary, providing an additional glimpse of intra-dot disorder. In Fig. A7, we observe a correlation of valley splitting between ground and excited orbitals, which is notably higher than between different dots in the same device (Fig. 4); this observation is highly suggestive of greater interface homogeneity on lengths akin to the spatial extent of single electrons (≈ 30 nm) compared to that of the distance between dots (≈ 150 nm). Curiously in most cases, the excited orbital valley splitting values are larger particularly when the ground valley splitting is small, which we attribute to systematic bias in resolving high energy peaks. As noted in Fig. 2(c), excited orbitals generally relax quickly and hence have faster inter-dot transition rates, broadening the associated DAPS peaks and making it difficult to identify small splittings in the vicinity of multiple orbital excitations.

Appendix H: Two-electron spectroscopy

While one-electron spectra are most transparent for understanding dot confinement, valley splitting, and decoherence pathways of single spins in dots, it is the energies of two-electron eigenstates that affect fidelities of the spin initialization and readout in spin qubit proposals. The DAPS technique can be readily applied to this case, and many useful variants can be envisioned. In particular, the singlet and triplet spectra of a two-electron

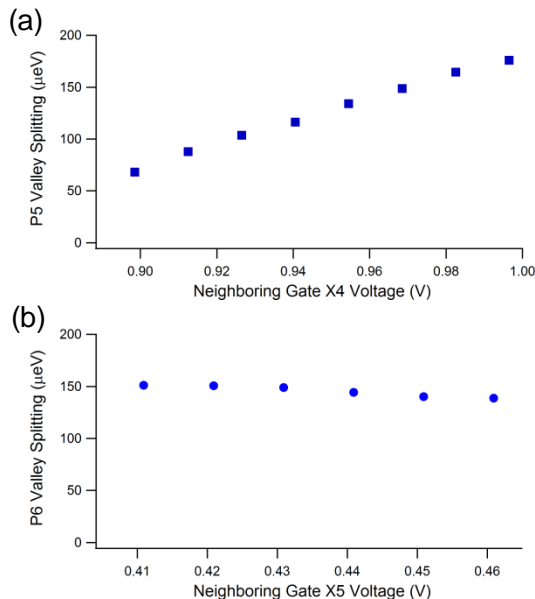


FIG. A6. Variation of valley splitting on either side of a P5-P6 DQD for a (a) P5 electron as function of bias on X4 and (b) P6 electron as function of bias on X5 gate.

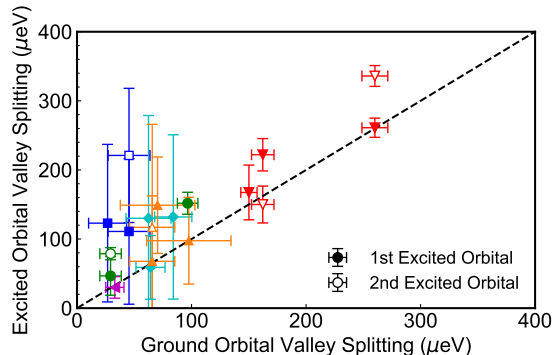


FIG. A7. Measurements of valley splitting in the ground, first, and second orbital states from six devices from five different wafers where each symbol color and shape corresponds same devices as in Fig. 4(a). Error bars are from Lorentzian fits of peak widths. Valley splittings of both the ground and first excited orbital states (solid) were measured on fifteen dots, while valley splittings of the second orbital states were measured on five dots (empty). The diagonal line is included for visual reference to indicate variations in valley splitting between different orbitals.

QD can be selectively probed in different ways using either a DQD or triple QD (TQD) device.

A simple DQD experiment could initialize a $(2,0)$ ground singlet, adiabatically separate it to the $(1,1)$ state, and then diabatically pulse along the detuning axis scanning for resonances with two-electron states of either one dot – when going towards $(2,0)$ – or the other – towards $(0,2)$. Due to spin conservation, this would predominantly probe singlets. This pulse sequence could be modified by adding a wait time $t_{dephasing}$ after adiabatic separation of the singlet. When $t_{dephasing}$ is comparable to the singlet-triplet dephasing lifetime T_2^* , both singlets and triplets should become accessible during the scan along the detuning axis. However, spectra crowding and conflicting optimal t_{Hold} values complicate extraction of state energies.

Alternatively, by introducing a third dot, we can form an exchange-only, TQD qubit [33, 50] that we can electrically manipulate to separately map out the two-electron singlet and triplet eigenstates of a singlet dot, as shown in Fig. A8. The sequence of steps for these experiments is very similar to that outlined above. As an example, the dots underneath plungers (P6,P5,P4) are operated around the $(2,0,1)$ - $(1,1,1)$ charge transition. A spin singlet is first initialized in the P6 dot and then adiabatically ramped into the $(1,1,1)$ charge cell. From this point, diabatic detuning pulses towards P6 result in two-electron eigenstates of the P6 dot (or P5 if going in the opposite direction along detuning axis) coming into and out of resonance with the P6/P5 $(1,1)$ singlet state. Dephasing at the anti-crossing points followed by a diabatic pulse back into the $(1,1,1)$ charge configuration results in a charge state-dependent outcome. The charge state mea-

surement is subtracted from the result in a second round of re-initialization followed by a charge state measurement. The resulting lock-in measurement for increasingly larger detuning pulses towards the P6 dot results in a series of peaks where the (1,1) singlet level crosses with the two-electron, spin-singlet eigenstates in P6. This measurement would be the same as in a DQD experiment, resulting in the orange line in Fig. A8(b) with pronounced singlet peaks. Additionally, in a TQD qubit a composite X_π Clifford gate using exchange pulses can be inserted after initialization to prepare a entangled three-spin state which projects only onto (1,1) P6/P5 triplet states. Subsequent diabatic detuning pulses into P6 then reveal only the resonances between the (1,1) triplets with two-electron spin-triplet eigenstates in P6 (Fig. A8(b), blue line). The spin-singlet and spin-triplet spectra of the P6 dot can be compared to determine whether valley or orbital states are limiting the lowest singlet-triplet energy splitting [29], and to assess the degree of valley-orbit coupling present in the dot.

Appendix I: State assignments of DAPS Spectra

Tables II and III contain the results from Lorentzian fits of the peaks seen in Fig. 3(a)-(b), from which the valley splittings presented in Table I are extracted. The rationale and caveats for the assignment of valley and orbital states are as discussed in the main text. Note

the substantially differing orbital splittings of P6 imply asymmetry in the confining potential.

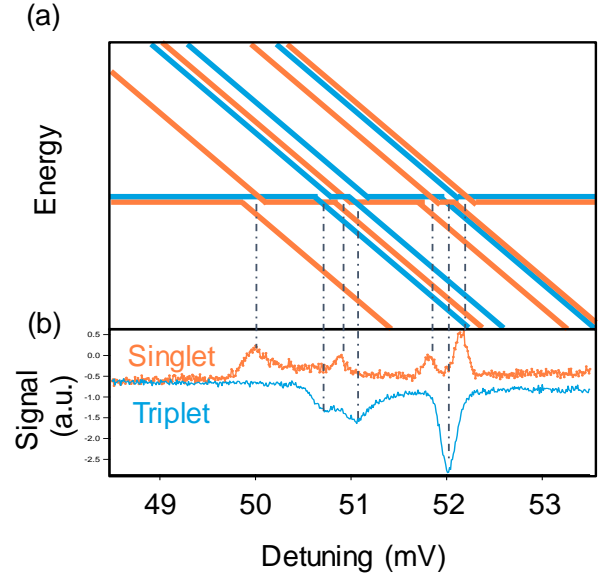


FIG. A8. (a) Schematics of 2-electron eigenenergies near (1,1)-(2,0) charge transition, allowing for valleys and excited orbitals. (b) Measured spin-dependent spectra of 2-electron states. Singlets in orange, triplets in blue.

TABLE II. Energy spectra of dot P5 from Fig. 3(a)

Orbital State	Lorentzian fit: Center \pm HWHM		Valley Splitting (μeV)
	Valley Ground (μeV)	Valley Excited (μeV)	
Ground	2 ± 7	-258 ± 9	260 ± 11
1st excited	$-1,184 \pm 14$	$-1,445 \pm 12$	261 ± 14
2nd excited	N/A ^a	$-1,520 \pm 13$	336 ± 15

^aPossibly overlapping with 1st excited orbital state.

TABLE III. Energy spectra of dot P6 from Fig. 3(b)

Orbital State	Lorentzian fit: Center \pm HWHM		Valley Splitting (μeV)
	Valley Ground (μeV)	Valley Excited (μeV)	
Ground	-1 ± 8	161 ± 6	162 ± 10
1st excited	$1,393 \pm 12$	$1,615 \pm 22$	222 ± 23
2nd excited	$2,125 \pm 23$	$2,275 \pm 26$	150 ± 27